Mon. Not. R. Astron. Soc. **000**, 000–000 (0000) Printed 10 May 2012 (MN LATEX style file v2.2)

Star formation in bulgeless late type galaxies: clues to their evolution

M.Das[1], C. Sengupta[2,3], S. Ramya[1], K. Misra[4]
1. Indian Institute of Astrophysics, Koramangala, Bangalore 560034, India
2. Instituto de Astrofsica de Andaluca (CSIC), Glorieta de Astronoma s/n, 18008 Granada, Spain
3. Calar Alto Observatory, Centro Astronmico Hispano Alemn, C/ Jess Durbn Remn, 2-2, 04004 Almeria, Spain
4. Space Telescope Science Institute, 3700 San Martin Drive, Baltimore, MD 21218, USA

Accepted.....; Received .....

ABSTRACT
We present GMRT 1280 MHz radio continuum observations and follow-up optical studies of the disk and nuclear star formation in a sample of low luminosity bulgeless galaxies. The main aim is to understand bulge formation and overall disk evolution in these late type galaxies. We detected radio continuum from five of the twelve galaxies in our sample; the emission is mainly associated with disk star formation. Only two of the detected galaxies had extended radio emission; the others had patchy disk emission. In the former two galaxies, NGC 3445 and NGC 4027, the radio continuum is associated with star formation triggered by tidal interactions with nearby companion galaxies. We did followup Hα imaging and nuclear spectroscopy of both galaxies using the Himalayan Chandra Telescope (HCT). The Hα emission is mainly associated with the strong spiral arms. The nuclear spectra indicate ongoing nuclear star formation in NGC 3445 and NGC 4027 which maybe associated with nuclear star clusters. No obvious signs of AGN activity were detected. Although nearly bulgeless, both galaxies appear to have central oval distortions in the R band images; these could represent pseudobulges that may later evolve into large bulges. We thus conclude that tidal interactions are an important means of bulge formation and disk evolution in bulgeless galaxies; without such triggers these galaxies appear to be low in star formation and overall disk evolution.

Key words: Galaxies:spiral - Galaxies:individual - Galaxies:nuclei - Galaxies:star formation - Galaxies:kinematics and dynamics - Galaxies:bulges - Galaxies:evolution - Galaxies:radio continuum.

1 INTRODUCTION

Bulgeless galaxies are an extreme class of late type spiral galaxiess (Scd to Sm) that have practically no bulge and are nearly pure disk in morphology (Böker et al. 2002). Although these galaxies are not rare their formation and lack of evolution remains a puzzle both for Cold Dark Matter (CDM) theories of hierarchical galaxy formation (White & Rees 1978), and the secular evolution theories of galaxy disks (Kormendy & Kennicutt 2004). The former process leaves clear signatures of merger history in the disks and the latter leads to the presence of oval distortions or disky bulges in the galaxy centers; neither of these features are seen in most bulgeless galaxies. One of the processes by which these disks could evolve is through interactions with nearby companion galaxies. The main aim of this work is to search for signs of such evolution by mapping the star formation and nuclear activity in a sample of nearby bulgeless galaxies. This can help us better understand the transformation of these predominantly disk dominated galaxies into bulge dominated systems.

Bulgeless galaxies show a wide variation in disk morphologies, ranging from the irregular dwarf galaxies to the nearly pure disk galaxies such as NGC 6503 (Kormendy et al. 2010). They are late type spirals and have large, gas rich disks with low to moderate star formation rates. In some cases their galaxy disks may be optically bright as in NGC 5457 (M 101), which has a relatively high star formation rate (Boissier et al. 2007). But most bulgeless galaxies have moderate to low surface brightness (LSB) disks, a good example being NGC 2552 which has a low luminosity disk (de Blok 2005). Being late type galaxies their dust content is often high (Popescu et al. 2002;Ganda et al. 2009;Boselli et al. 2012) and this can lead to significant optical extinction. Although bulgeless, small bars and oval distortions may be present as well as flocculent spiral arms that result in localized disk star formation. Such features are much lower in the more isolated bulgeless galaxies (Kautsch 2009, e.g.). The large scale spiral arms and bars that signify strong disk instabilities are not seen in most of bulgeless galaxies, especially the low luminosity (LL) ones. This suggests that they may have dominant dark matter halos that stabilise their disks against the formation of bars, spiral arms or oval perturbations. Indeed, for the LSB bulgeless galaxies this is the case (Zackrisson et al. 2006; Banerjee et al. 2010) but this may also be true for the brighter bulgeless galaxies as well (Salucci & Persic 1997; Kormendy & Freeman 2004). Hence, only nearby interactions may be able to trigger disk instabilities that will lead to star formation, nuclear gas inflow and central mass buildup in these

galaxies. It is these processes that could result in bulge formation in such systems.

The formation and evolution of bulgeless galaxies in a ΛCDM universe is not well understood. Their angular momentum and rotation velocities are not unusual for late type systems (Matthews & Gallagher 2002), but are too high to be compatible with CDM models of galaxy formation (D'Onghia & Burkert 2004). Some models suggest that galactic outflows due to supernovae and stellar winds can remove low angular momentum material from these disks leaving behind higher angular momentum material in the disks (Brook et al. 2011; Governato et al. 2010). Or hot gas during the merging epoch is redistributed back to the disk via a galactic fountain (Brook et al. 2012). However, this process may not explain the nearly pure disk morphology for the larger bulgeless galaxies, especially those that are relatively low in star formation actvity. Thus, although dynamically these galaxies represent the simplest form of disk galaxies, the physics behind their simple form is far more challenging to understand.

Apart from the challenge of forming such pure disk galaxies, there is also the question of how they develop nuclear black holes and active galactic nuclei (AGN). Galaxy bulges and AGN are thought to grow together in the nuclei of galaxies (e.g. Silk & Rees 1998; Daddi et al. 2007) and most AGN in our nearby Universe are associated with bulges (e.g. Heckman et al. 2004). But suprisingly AGN have been detected in the nuclei of bulgeless galaxies (Filippenko & Ho 2003; Satyapal et al. 2007; Gliozzi et al. 2009; Satyapal et al. 2009). Perhaps the most well studied example is NGC 4395 (Filippenko et al. 1993). The galaxy has a Seyfert 1 nucleus that has a black hole of mass $\sim 10^5\ M_\odot$ (Peterson et al. 2005; Peterson et al. 2005) which puts it in the intermediate mass black holes (IMBH) domain. In fact most of the AGN detected in bulgeless galaxies have been found to be associated with IMBHs (McAlpine et al. 2011; Shields et al. 2008). It is not clear where these galaxies lie on the $M-\sigma$ correlation as they barely have a bulge; or how to explain their AGN activity which should be correlated with the formation of a bulge. Recent studies indicate that the SMBHs do not correlate with the disks or pseudobulges in galaxies (Kormendy et al. 2011), hence the disk may not be directly correlated with the growth of nuclear black holes in bulgeless galaxies. The AGN found in these galaxies are often buried inside nuclear star clusters which appear as bright cores in place of bulges (Böker et al. 2002; Böker et al. 2004; Walcher et al. 2005; Seth et al. 2008; Neumayer et al. 2011).

In this paper we investigate how star formation and nuclear activity in bulgeless galaxies can result in bulge formation disk evolution such galaxies. We focus only on LL bulgeless galaxies that may or may not have a bar, but do not have a prominent bulge. We use radio observations to map the star formation and search for compact nuclear emission in our sample of twelve galaxies. Radio emission has the advantage that it is not affected by dust obscuration and hence in this case may be a better tracer of the star formation. For a deeper understanding we have followed up two interesting cases with optical spectroscopy and Hα imaging observations. In the following sections we discuss our sample, the observations and our results. We then summarise our findings and discuss their implications.

2 GALAXY SAMPLE

Our sample consists of twelve late type LL spiral galaxies (Table 1) that appear to be bulgeless or have a minimal bulge in their Hubble Space Telescope (HST) Wide Field and Planetary Camera 2 (WFPC2) images (Böker et al. 2003). The galaxies have a range of disk morphologies; some have nearly pure disks and some have progressively more distinct centers that may represent bulges in early stages of evolution. They all have compact stellar cores as indicated by their HST I band light profiles and are detected at some level in their NRAO VLA Sky Survey (NVSS) radio maps. However, the resolution of NVSS is poor (45″) and hence does not show the detailed radio morphology. Only six galaxies have Very Large Array (VLA) Faint Images of the Radio Sky at Twenty Centimeters (FIRST) radio maps; UGC 4499, NGC 3445, NGC 3782, NGC 3906, NGC 4701 and NGC 5584. FIRST has a smaller beam size (5″) and so the higher resolution is able to pick up the more intense emission that maybe associated with star formation. Of these six FIRST galaxies, only NGC 4701 shows radio emission and it is associated with the inner disk. In the following paragraph we briefly describe our sample galaxies.

ESO 418-8, NGC 4299, NGC 4540 and UGC 4499 : All four galaxies have fairly featureless disks that do not support recent large scale star formation or spiral structure. Only knotty or very localised star forming regions are seen in the optical and UV maps (Gil de Paz et al. 2007). The NVSS maps reveal extended but relatively weak radio emission from the disks and is probably associated with the localized star forming regions.

NGC 3346 and NGC 5668 : Both galaxies are relatively nearby and nearly face-on in orientation. NGC 3346 has a small bar in the center that is associated with a fairly strong spiral structure. NGC 5668 has less prominent spiral structure. The NVSS maps shows diffuse and extended radio emission distributed over the inner disks of both galaxies.

NGC3445 : Optical images suggest that this is a one armed spiral galaxy. The prominence of the southern spiral arm gives the galaxy a lopsided appearance; only a closer inspection of the 2MASS K band image reveals the smaller northern arm. NGC 3445 forms part of a triplet of galaxies with two other galaxies, NGC 3440 and NGC 3458. Close to the southern arm and lying east of the nucleus of NGC 3445, there is a prominent star forming region that may have formed from a retrograde encounter with a neighbouring galaxy (Cao & Wu 2007). GALEX observations of the galaxy show that the star formation is extended over the disk (Smith et al. 2010) though much of it is associated with the spiral arms and the nucleus. The galaxy has a bright nucleus that hosts a nuclear star cluster (Seth et al. 2008) but no AGN. The radio flux in the NVSS maps is large compared to other galaxies in our sample but due to the poor resolution of NVSS, not much can be said about the radio morphology. This is one of the few galaxies in our sample that has been detected in CO emission (Böker et al. 2003); the molecular gas mass is relatively low and centrally concentrated. The galaxy has a small oval bar in the center but bulge-disk separation was not possible in this galaxy, perhaps because the 'bulge' is too small (Baggett et al. 1998).

NGC 3782 and NGC 3906 : Both galaxies have small bars in their centers but no strong spiral structure. Knots of star formation are distributed over their disks. The radio emission is diffuse and extended over the galaxy disks. NGC 3782 is fairly inclined ($i = 60^\circ$) but NGC 3906 is close to face-on in morphology.

NGC 4027 : This galaxy, like NGC 3445, appears to be a one armed spiral galaxy in the optical images; this is mainly due to the prominent northern spiral arm that gives it a lopsided appearance. The smaller southern spiral arm appears much more prominent in the HI images of the galaxy (Phookun et al. 1992) and extends down towards the smaller companion galaxy NGC 4027A. The net ef-

Table 1. Galaxy Sample and Parameters

Galaxy	Other Name	Type	Distance (Mpc)	Position (RA, DEC)	Velocity (km s^{-1})	Optical Size	NVSS Radio Emission (mJy)
ESO 418-8	PGC 013089	SB(r)d	14.9	03h31m30.6s, -30d12m48s	1195	1.2’	3.8
UGC 4499	PGC 024242	SABdm	11.5	08h37m41.5s, +51d39m09s	691	1.99’	2.0
NGC 3346	UGC 05842	SB(rs)cd	22	10h43m38.9s, +14d52m19	1260	2.7’	13.8
NGC 3445	UGC 06021	SAB(s)m	30.8	10h54m35.5s, +56d59m26s	2069	1.6’	23.6
NGC 3782	UGC 06618	SAB(s)cd	13.2	11h39m20.7s, +46d30m50s	739	1.7’	4.6
NGC 3906	UGC 06797	SB(s)d	16.1	11h49m40.5s, +48d25m33s	961	1.9’	2.0
NGC 4027	PGC 037773	SB(s)dm	27.9	11h59m30.2s -19d15m55s	1671	3.2’	91.0
NGC 4299	UGC 07414	SAB(s)dm	7.79	12h21m40.9s, +11d30m12s	232	1.7’	17.2
NGC 4540	UGC 07742	SAB(rs)cd	22.1	12h34m50.8s, +15d33m05s	1286	1.9’	3.1
NGC 4701	UGC 07975	SA(s)cd	14.5	12h49m11.6s, +03d23m19s	721	2.8’	18.5
NGC 5584	UGC 09201	SAB(rs)cd	26	14h22m23.8s, -00d23m16s	1638	2.45’	19.4
NGC 5668	UGC 09363	SA(s)d	25	14h33m24.3s +04d27m02s	1582	3.3’	23.5

fect of the tidal interaction between NGC 4027 and NGC 4027A has resulted in an extended HI ring around NGC 4027. The star formation is distributed over the disk and and especially along the spiral arms of NGC 4027. The 1.4 GHz radio continuum flux for this galaxy is the highest in the sample (Table 2) and the emission is distributed over the disk and nuclear regions. The molecular gas mass of this galaxy is suprisingly low (Young et al. 1995) and less than 6×10^6 M$_\odot$ (Das et al. 2005); it is close to the detection limits in the FCRAO survey. This is also the only galaxy in our sample that has a very small bar that appears as an oval distortion in the center of the galaxy (Phookun et al. 1992). Its bulge to disk size is very low (1/25) (Baggett et al. 1998) which suggests that it may be a pseudobulge or a bulge in early stages of formation.

NGC 4701 and NGC 5584 : Both galaxies have a small bright nucleus and a flocculent spiral structure. Star formation is associated with the spiral pattern. The NVSS images show extended but diffuse radio emission from the disks and is probably associated with star forming regions over the spiral arms. NGC 4701 also shows some emission in the higher resolution FIRST radio map. The emission is concentrated about the nucleus and the inner disk.

3 RADIO OBSERVATIONS

We observed the galaxies in radio continuum at 1280 MHz using the Giant Meterwave Radio Telescope (GMRT) located near Pune, India (Ananthakrishnan & Rao 2002). Observations were done during May, 2008. Nearby radio source were used for phase calibration. Each galaxy had a two hour scan; excluding time spent on nearby calibrators the average on source time was about 1.5. The data was obtained in the native ”lta” format, converted to FITS format and then analysed using AIPS [1]. Bad data was iteratively edited and calibrated on a single channel until satifactory gain solutions were obtained using standard tasks in AIPS. This was used to generate bandpass solutions. The central 110 channels were bandpass calibrated and averaged to obtain the continuum database. This was then imaged using IMAGR. Both natural and uniform weighted maps of the galaxies were made to obtain the extended structures and see if there is any compact emission associated with the nuclei (Figures 1-5). We also experimented with different UV tapers to bring out the extended, fainter radio emission.

4 Hα IMAGING AND OPTICAL SPECTROSCOPY OF NGC 3445 AND NGC 4027

We did Hα imaging and optical spectroscopy of the two galaxies, NGC 3445 and NGC 4027, that showed extended emission in the GMRT radio continuum maps. The observations were done with the 2m Himalayan Chandra Telescope (HCT) which is located at the Indian Astronomical Observatory (IAO) at Hanle. The telescope is remotely controlled from the Center for Research and Education in Science and Technology (CREST) which is part of the Indian Institute of Astrophyiscs (IIA) in Bangalore. The spectrum of NGC 3445 was obtained on a cloudless night on 17 March 2010 and NGC 4027 was observed on a clear night on 19 January 2010. The spectra were obtained using a $11' \times 1.''92$ slit (#167l) in combination with a grism #7 (blue region) and grism #8 (red region) which covers the wavelength ranges 3700–7600 Å and 5500–9000 Å with dispersions of 1.46 Å pixel^{-1} and 1.26 Å pixel^{-1}, respectively. The spectral resolution is around $\sim$ 8.7 Å (398 km s^{-1} FWHM or σ = 169 km s^{-1} at Hα) for grism #7 and $\sim$ 7 Å (σ = 136 and 103 km s^{-1} at Hα and Ca II Triplet respectively) for grism #8. The spectra were obtained after exposing both the galaxies for about 2400 s in grism #7. The spectrum of NGC 4027 in grism #8 was obtained with an exposure of 1800 s. Due to the low signal to noise (S/N) ratio of the grism #8 spectrum of NGC 3445, we did not use it for further analysis. The slit was placed at the centre of the galaxy covering a central region of $\sim 2'' \times 5''$ ($1''$ corresponds to 135 pc at a redshift of $\sim$ 0.0055).

Data reduction was carried out using the standard tasks available within IRAF [2] which includes bias subtraction, extraction of one dimensional spectra, wavelength calibration using the ferrous argon lamp for grism #7 and ferrous neon lamp for grism #8. The wavelength calibrated spectra were flux calibrated using one of the spectroscopic standards of Oke (1990) observed on the same night and then corrected for the redshifts of the galaxies. The blue and the red flux calibrated spectra of NGC 4027 were combined together

[1] Astronomical Image Processing System (AIPS) is distributed by NRAO which is a facility of NSF and operated under cooperative agreement by Associated Universities, Inc.

[2] Image Reduction & Analysis Facility Software distributed by National Optical Astronomy Observatories, which are operated by the Association of Universities for Research in Astronomy, Inc., under co-operative agreement with the National Science Foundation

Table 2. FIR-Radio ratio (q) and Star Formation Rate for Galaxies Detected in Radio Emission

Galaxy Name	Far-infrared flux ($W\ m^{-2}$)	q value	Star Formation Rate ($M_\odot\ yr^{-1}$)	GMRT Radio Emission at 1.28 GHz (mJy)	Beam Size ($''$)
NGC 3445	12.16	2.14	1.2	12.0 ± 3.3	8
NGC 3782	6.86	2.28	0.2	10.3 ± 3.9	45
NGC 4027	74.79	2.34	4.2	77.5 ± 10.9	8
1 NGC 4299	18.75	2.46	...	4.1 ± 1.9	7
NGC 5668	15.43	2.24	...	4.0 ± 2.2	39

[a] FIR flux ($W\ m^{-2}$) = $1.26 \times 10^{-14}[2.58\ S_{60} + S_{100}]$
[b] q = $\log[\frac{FIR}{3.75\times10^{12}}/S_{1.4\ GHz}]$
[c] Star formation rate derived from the total infra-red luminosities of the galaxies (L_{TIR}) listed in Bell (2003) by using the relation for SFR also listed in the paper i.e. SFR ($M_\odot\ yr^{-1}$) = $1.72\times10^{-10}L_{TIR}(1 + \sqrt{\frac{10^9}{L_{TIR}}})$.
[d] GMRT fluxes were derived from the natural weighted or low resolution maps. The errors were derived from the noise in the maps (in units of mJy/beam) and the beam size.

with the help of *scombine* within *specred* package using a suitable scale factor estimated at the flat continuum portions of the overlapping part of the spectra. The flux calibrated spectra of NGC 3445 and NGC 4027 are shown in Figures 10 and 12.

The Hα images of NGC 3445 and NGC 4027 were obtained on 17 March 2010 from HCT. The Hα filter installed inside the Himalaya Faint Object Spectrograph system (HFOSC) is centered around 6550 Å and has a bandwidth of 100 Å. Bessells *R* filter (centered around 6400 Åwith a BW of ∼ 1600 Å) is used for continuum subtraction similar to the procedure described in Waller (1990). As discussed by James et al. (2004), for dark nights, the scaled *R* band exposure gives an excellent continuum subtraction. Each of the Hα frames was observed for 10 minutes. Sky subtracted unit exposure time *R* frame was scaled and subtracted out from the Hα that was also sky subracted and normalized with respect to exposure time. The final continuum subtracted Hα frames for two galaxies NGC 3445 and NGC 4027 are shown in the Figures 6 and 7, respectively.

5 RESULTS

5.1 Radio Observations

We have detected radio emission from five of the twelve galaxies in our sample (Table 2). Although all twelve galaxies have radio emission in the NVSS images, only five were detected in our study. There are several reasons for this : 1. Some of the sources have NVSS flux which is extended and diffuse disk emission. These sources had low level flux (2 to 3 mJy) in NVSS, which is close to NVSS noise value. With GMRT we confirmed that they are non-detections e.g. ESO 418, NGC4499, NGC3906, NGC4540. 2. Our GMRT observations were only two hours scans of each source. Hence, the UV coverage is not very high. Deeper observations are required to detect the more diffuse emission. Hence only emission with high flux density is detected. A good example is NGC 4027 where the GMRT and NVSS fluxes are close in value. 3. In some cases, such as NGC 3782, the GMRT flux is much less than the NVSS flux because of confusion with a much brighter source nearby. Since the NVSS beam is large, this emission from a nearby source is picked up. 4. In one galaxy, NGC 4701, the data quality is not good enough (too noisy) to detect the source even though the FIRST map shows some emission close to the nucleus. In some cases, heavy flagging was needed for the central baselines; this along with incomplete UV coverage, led to non detections or flux loss.

In the following paragraphs we discuss our results in more detail. The GMRT flux is quite high for the galaxies NGC 3445 and NGC 4027 and the NVSS and GMRT fluxes are comparable. In these galaxies the radio emission is extended and associated with massive star formation along the spiral arms. Interestingly, both these galaxies are also tidally interacting with nearby companion galaxies.

(i) NGC 3782, NGC 4299, NGC 5668 : All three galaxies show only patchy radio emission associated with the disk (e.g. Figure 1; NGC 4299) and is due to localized star formation. Thus although the galaxies show extended radio emission at 1.4 GHz in the NVSS maps, our higher resolution GMRT observations could only detect small pockets of localized emission. This suggests that unlike NGC 3445 and NGC 4027, there is not much ongoing high mass star formation in these galaxies.

(ii) NGC 3445 : The radio emission mainly follows the prominent southern spiral arm (Figure 2) and to some extent the less prominent northern arm. It is due to thermal emission associated with star formation triggered by tidal interactions with the companion galaxies NGC 3440 and NGC 3458 (Smith et al. 2007). The peak flux detected in our observations is 2 mJy/beam (where the beam is $8''$ and map noise is 0.15 mJy/beam) and is coincident with the large star forming region south of the galactic nucleus. The total radio emission that we detect at 1280 MHz with the $8''$ beam is 11.3 mJy which is about half of the the flux detected at 1420 MHz by NVSS which has a much larger beam (Table 2). In the high resolution or uniformly weighted map (Figure 3) the emission breaks up into two peaks. The brighter peak is associated with the southern spiral arm and the other lies along the northern spiral arm. Suprisingly there is no emission associated with the nucleus even though this galaxy does have a prominent nuclear star cluster (Seth et al. 2008). We calculated the star formation rate from the total infra-red luminosity (TIR); its value is ≈ 1 $M_\odot\ yr^{-1}$ (Bell 2003). Although this is not high it is significant for a relatively low luminosity galaxy. NGC 3445 is also one of the few galaxies in our sample that has molecular hydrogen gas (Böker et al. 2003); it is mainly confined to the inner parts of the galaxy disk and is probably associated with the disk star formation.

(iii) NGC 4027 : This galaxy shows the maximum radio emission in our sample (Figure 4). The net flux is ∼ 88 mJy and is mainly

Table 3. Hα luminosities and Star Formation Rates for Individual Regions in NGC 3445 and NGC 4027

Galaxy	Region	Hα Luminosity (10^{41}erg s^{-1})	Star Formation Rate ($M_\odot\ yr^{-1}$)	Number of O stars
NGC 3445	1	1.62	1.29	1.2×10^4
	2	0.18	0.14	1.3×10^3
	3	0.17	0.14	1.3×10^3
	4	0.10	0.08	0.7×10^3
NGC 4027	1	0.73	0.58	5.4×10^3
	2	0.29	0.23	2.1×10^3
	3	0.74	0.59	5.4×10^3
	4	2.04	1.62	1.5×10^4
	5	0.58	0.46	4.2×10^3
	6	0.37	0.30	2.7×10^3
	7	0.91	0.72	6.7×10^3
	8	0.71	0.56	5.2×10^3

[a] Star formation rate ($M_\odot\ yr^{-1}$) = L(Hα)/(1.26×10^{41}erg s^{-1}) (Kennicutt 1998)

[b] Approximate number of O stars determined from number of ionizing photons $N_{Lyc}=7.34\times10^{11}$L(H$\alpha$) photons s^{-1} where we have assumed the rate of ionizing photons from one O5 star to be 10^{49} photons s^{-1} (Ravindranath & Prabhu 1998).

distributed around the southern spiral arm. The emission north of the galaxy center is patchy and does not follow the spiral pattern as closely as the southern arm. The emission along the southern spiral arm is concentrated at two locations. There is also some emission associated with the galaxy nucleus; it could be due to nuclear star formation or weak AGN activity. In the high resolution map (Figure 5) most of the emission is associated with the southern arm which indicates that the more intense star formation is located in this part of the galaxy. There is also emission associated with the galaxy nucleus; it may be due to the nuclear star cluster (Seth et al. 2008) or a weak AGN. We determined the star formation rate from the total infra-red luminosity and its value is $\approx$ 4 $M_\odot\ yr^{-1}$ (Bell 2003). The radio morphology clearly indicates that star formation activity has been triggereed by the tidal interaction with the smaller galaxy NGC 4027A that lies south of the galaxy and closely follows the large HI ring that envelopes both galaxies. Suprisingly, the northern spiral arm is more prominent in the optical images than the southern arm. This could be due to the orientation of the galaxies during the interaction. Hence the northern spiral arm is comprised of older stars due to previous star formation activity whereas the southern arm represents ongoing star formation in NGC 4027.

5.2 Hα imaging of NGC 3445, NGC 4027 and the Residual R Images

The Hα emission maps of NGC 3445 and NGC 4027 are shown in Figures 6 and 7. The main emission regions are circled in red. We have determined the Hα flux for these knots and estimated the star formation rate for these regions using the empirical relation of Kennicutt (1983); the values are listed in Table 3. We have also obtained the Hα subtracted R band images of the galaxies and examined the core structure in both galaxies.

NGC 3445 : The distribution of Hα emission in NGC 3445 follows the UV emission quite closely as seen in the GALEX images (Gil de Paz et al. 2005;Smith et al. 2010). There are two knots of star formation concentrated along the spiral arms; one lies north of the galactic nucleus and the second, which is much larger, lies southwest of the nucleus (Figure 6). The radio emission also closely follows the Hα emission as seen in the overlay (Figure 8). We did not detect any Hα emission from the nucleus; only emission from star forming regions in the tidally interacting arms is observed. The radio continuum peak at 1280 MHz coincides with the strong HII regions located at the western and northern regions. Table 3 shows the Hα luminosities for the more prominent star forming knots as well as their respective star formation rates (SFR). The SFR is less than 1 $M_\odot\ yr^{-1}$ for most regions except the large star formation knot located in the southern arm which has a SFR of $\approx$1.5 $M_\odot\ yr^{-1}$.

NGC 4027 : The Hα emission observed in NGC 4027 (Figure 7) is much higher than that observed in NGC 3445 and the FIR luminosity (Table 2) is also higher. This is probably because the rate of newly forming stars is closely related to the tidal interaction with the companion galaxy and the tidal interaction in NGC 4027 (Phookun et al. 1992) appears to be stronger than that in NGC 3445. The Hα emission in NGC 4027 closely follows the spiral arms but is more concentrated along the southern arm where there are two large knots of star formation; these are clearly seen in the radio map overlay (Figure 9). As in NGC 3445, the peak of the 1280 MHz radio emission coincides with the strong HII region complexes in the spiral arms. Using luminosity of each of the knots we have derived the star formation rates (Table 3); the number of O stars present in each of the knots is also given in the Table 3 and lies in the range 10^2 to 10^4. There is also Hα emission associated with the nucleus which could be due to nuclear star formation and possibly an AGN (see next subsection).

Residual R band Image : The Hα subtracted residual R band images are not very deep but give an idea of the disk structure in both galaxies (e.g. Figure 10, NGC 4027). We used the iraf task *ellipse* to fit ellipses and examine whether there are oval distortions in the galaxy centers. NGC 4027 has an oval distortion of ellipticity approximately 0.6 and position angle 83°. The size of the oval distortion is $\approx 15''$ or 0.65 kpc. The structure is disky rather than spherical and suggests that it may be a pseudobulge that has formed from the buckling of a much smaller bar and is in the process of growing into a bulge (Sellwood & Wilkinson 1993). The bulge-disk decomposition of NGC 4027 yields a bulge scale length of $r_e \sim 1''$ and disk $\mu_e \sim 16.2''$ (Baggett et al. 1998). The bulge size is much smaller than our estimate using ellipse fitting; perhaps because their decomposition measures the central core and not the whole oval structure. The R image of NGC 3445 also has a small bulge in its center but it is not as elliptical as the incipient "bulge"

in NGC 4027. The oval distortion in NGC 3445 appears to have an ellipticity less than 0.5 and a position angle 45°; the total size is less than 0.5 kpc. The bulge is too small for bulge disk decomposition (Baggett et al. 1998). The images also show that both galaxies have spiral arms that are associated with the tidal interactions with nearby galaxies. The spiral structure is sharper in NGC 4027 than NGC 3445; possibly because the tidal interaction is stronger in NGC 4027 (Phookun et al. 1992).

5.3 Optical spectroscopy of NGC 3445 and NGC 4027

(i) NGC 3445 : The optical spectrum of NGC 3445 is displayed in Figure 11. The fluxes of emission lines are tabulated in the Table 4. A strong underlying stellar population in absorption is detected at Hβ , Hγ and Hδ wavelengths. The composite light from NGC 3445 is decomposed using an underlying stellar spectrum, an Fe II template and a power-law continuum using a the Levenberg-Marquardt χ^2 minimization technique. The procedure followed is discussed in detail in Ramya et al. (2011). The spectrum of NGC 3445, the decomposed components and the model subtracted final spectrum are all plotted in Figure 12. The age of the underlying stellar population is estimated to be in the range 500 Myr to 1 Gyr indicating that a recent episode of star formation has occurred in the galaxy. The galaxy is also experiencing current episodes of star formation as seen from the Hα images. We searched for signatures of hidden AGN activity but no broad Hα emission line was detected even after subtracting the underlying stellar continuum. NGC 3445 is classified as a galaxy with nuclear star clusters (Seth et al. 2008) rather than hosting an AGN or a composite kind of nucleus. We investigated where NGC 3445 lies on the Baldwin, Phillips & Terlevich (BPT) diagram; the values of log(ø3 λ5007/Hβ)$\sim$ 0.18 and log([N II] λ6584/Hα)$\sim$ $-$0.62 lie in the region occupied by star forming galaxies. The fluxes of emission lines (see Table 4) were used to calculate ionic abundances of each of the species of O, N, S using the task IONIC from the STSDAS package of IRAF. The electron temperature and density are $\sim$ 11107 K and $\sim$ 26 cm^{-3}, respectively. The elemental abundances are estimated following the prescription of Pilyugin et al. (2010). The oxygen abundance 12 + log($\frac{O}{H}$) = 8.4 and nitrogen abundance is estimated to be 12 + log($\frac{N}{H}$) = 7.56. The metallicity is only slightly less than solar (12 + log($\frac{O}{H}$) = 8.67) metallicity in value.

(ii) NGC 4027 : The spectrum of NGC 4027 is displayed in Figure 13. It is interesting to note that the spectrum does not show any forbidden lines of Oxygen like [O II] λ3727, ø3 $\lambda\lambda$4959,5007 or even [O I] λ6300. The non-detection of oxygen lines but presence of [N II] $\lambda\lambda$6548,6584 and [S II] λ 6717,6731 is surprising. It could be due to dust (Roussel et al. 2001) which may have used up most of the oxygen during the formation of dense clouds. Also, the Balmer decrement (Hα/Hβ) is approximately 6, which is much greater than the theoretically expected value of 3. Table 5 displays the emission line fluxes, equivalent widths, and ionic abundances. In comparison with NGC 3445, the nitrogen and sulphur ionic abundances of NGC 4027 are higher by about 0.6 dex and 0.1 dex, respectively, which hints towards higher oxygen abundance and metallicity than NGC 3445. The stellar decomposition was carried out and the residual spectrum, Figure 14, neither shows any oxygen line nor show any broad Hα emission confirming that this galaxy hosts a nuclear star cluster and not an AGN (Seth et al. 2008). The age of the underlying stellar population as estimated from the best fit starburst99 template is $\sim$ 1 Gyr. Using the emission line ratio of [S II] λ 6717/6731, the electron density is estimated to be 273 cm^{-3}.

6 DISCUSSION

(i) Star Formation in Bulgeless Galaxies : Our radio observations as well as general observations in the literature suggest that bulgeless galaxies are generally poorly evolved systems that have low star formation rates (SFR) unless interacting with nearby galaxies (Kautsch 2009). In our study all the galaxies are rich in HI (Watson et al. 2011) and hence have the capacity to support star formation, but most are fairly quiescent. We compared our galaxies with other pure disk galaxies that have been studied in the literature; such as the relatively low luminosity galay NGC 6503 and the brighter galaxy M101. We estimated their SFRs using the total infrared (TIR) luminosities (Bell 2003) as we did for our sample galaxies in Table 2. NGC 6503, which has a low SFR of 0.22 $M_\odot\ yr^{-1}$, is close to the local void (Karachentsev et al. 2003) and is hence fairly isolated. Its SFR is similar to NGC 3782 which shows only patchy star formation. M101 (NGC 5457), however, is a fairly bright star forming spiral and has a SFR 4.1 $M_\odot\ yr^{-1}$; it is part of a group of mainly dwarf galaxies (Kinney et al. 1993). Its SFR is similar to NGC 4027 but larger than NGC 3445; the star formation is probably triggered by interactions with nearby galaxies in the group. These two examples also suggest that bulgeless galaxies are generally low in star formation unless interacting with nearby galaxies. This raises the possibilty that their disks are more dark matter dominated than regular spirals and hence need a strong trigger, such as an interaction with a close companion galaxy, to start forming stars.

(ii) Bulge growth in disk dominated galaxies : The main result of this work is that we have found two cases of ongoing bulge formation in two low luminosity bulgeless galaxies, NGC 3445 and NGC 4027 in which bulge formation has been triggered by close tidal encounters with nearby galaxies. Both galaxies are dark matter dominated systems since they are late type spirals with low luminosity disks (Salucci & Persic 1997). Such systems are not easily perturbed to form bars and spiral arms. However, interaction induced disk activity can result in enhanced star formation that can eventually lead to the build-up of bulges in the galaxy disks (Kormendy & Fisher 2008). This process may be ongoing in NGC 3445 where a small bright core or bulge maybe developing. Alternatively, tidal interaction can trigger bar formation and this can lead to bulge growth through the formation of a pseudobulge. This may have happened in the case of NGC 4027 where the small oval distortion that we see in the R band image may have started out as a small bar instabilty; this then buckled to form an oval distortion or pseudobulge (Combes et al. 1990;Raha et al. 1991;Martinez-Valpuesta & Shlosman 2004). Another example of interaction induced activity in a LL galaxy is NGC 4625. This galaxy is interacting with NGC 4618 and perhaps merging with NGC 4625A (Gil de Paz et al. 2005); the close interaction has triggered star formation in the extended low surface brightness (LSB) disk of NGC 4625. Thus, close tidal encounters are an important mechanism for the evolution of halo dominated systems such as LSB galaxies or low luminosity bulgeless galaxies such as those in our study.

(iii) AGN-bulge evolution : The well known black hole mass and bulge velocity relation (Ferrarese & Merritt 2000; Gebhardt et al. 2000; Gültekin et al. 2009) is difficult to understand in the context of bulgeless galaxies, since it implies that black hole growth is very difficult without a bulge. However, there is a significant number of bulgeless galaxies that show AGN activity and have intermediate mass black holes (IMBH), for example NGC 3367 and NGC 4536 (McAlpine et al. 2011). Kormendy et al. (2011) have suggested that

Table 4. Emission line intensities, ionic abundances and elemental abundances of atomic species obtained from spectra of the galaxy NGC 3445.

Species	Wavelength λ	Flux [a]	EqW Å	Ionic $\frac{X^+}{H^+}$	Abundance $12 + \log(\frac{X^+}{H^+})$
[O II]	7325	7.08056	-0.809	1.053 E-4	8.46
[N II]	6548	42.367	-2.815	1.881 E-5	7.71
Hα	6563	473.356	-32.12	—	—
[N II]	6584	109.445	-7.645	1.652 E-5	7.65
[S II]	6717	84.1673	-6.068	2.568 E-6	6.84
[S II]	6731	58.6366	-4.286	2.495 E-6	6.83
He I	5876	17.9532	-1.052	—	—
Hβ	4861	100	-5.444	—	—
ø3	4959	56.5241	-3.072	4.117 E-5	8.05
ø3	5007	158.82	-8.831	4.003 E-5	8.04
Hγ	4340	23.4057	-1.349	—	—
[O II]	3727	343.514	-23.39	0.819 E-4	8.35
F(Hβ) erg cm^{-2} s^{-1}				1.97×10^{-14}	
12+log($\frac{O}{H}$)				8.40[b]	
12+log($\frac{N}{H}$)				7.56[b]	

[a] Fluxes of all species are normalised with respect to Hβ flux and errors on the fluxes are in the range 5 – 10%.
[b] The oxygen and nitrogen abundances are estimated using the new calibration of Pilyugin et al. (2010).

Table 5. Emission line intensities, ionic abundances and elemental abundances of atomic species obtained from spectra of the galaxy NGC 4027.

Species	Wavelength λ	Flux [a]	EqW Å	Ionic $\frac{X^+}{H^+}$	Abundance $12 + \log(\frac{X^+}{H^+})$
[O II]	7325	—	—	—	—
[N II]	6548	108.77	-4.65	6.29 E-5	8.23
Hα	6563	671.07	-29.22	—	—
[N II]	6584	304.19	-13.58	5.98 E-5	8.21
[S II]	6717	88.20	-3.60	3.91 E-6	7.03
[S II]	6731	74.98	-3.06	3.91 E-6	7.03
He I	5876	33.66	-1.20	—	—
Hβ	4861	100	-3.71	—	—
ø3	4959	—	—	—	—
ø3	5007	—	—	—	—
Hγ	4340	—	—	—	—
[O II]	3727	—	—	—	—
F(Hβ) erg cm^{-2} s^{-1}				1.37×10^{-14}	

[a] Fluxes of all species are normalised with respect to Hβ flux and errors on the fluxes are in the range 5 – 10% because of poor signal-to-noise of the optical spectrum.
[b] Since oxygen lines are undetected in the spectrum of NGC 4027, it was not possible to estimate the oxygen and nitrogen abundances.

there are two ways of forming nuclear black holes; one driven by mergers and gas infall; it leads to the formation of classical bulges and is often associated with SMBHs in massive galaxies. The second is through secular evolution processes the galaxy disks; this includes the formation of bars and pseudobulges. This latter process leads to the formation of smaller black holes or IMBHs in the centers of galaxies. In our study, NGC 3445 may be in the process of forming a bulge through the first process, i.e. gas infall and central star formation whereas NGC 4027 may be an example of the second mode of bulge growth. In NGC 4027 the formation of spiral arms and the growth of a central bar has been triggered by close tidal interactions with the nearby galaxy NGC 4027 A, leading to the formation of a pseudobulge (Figure 10) and weak AGN activity. Although neither NGC 3445 or NGC 4027 show optical emission lines characteristic of AGN, the AGN activity may star later. Studies indicate that the nuclear black holes begin to accrete and show AGN activity only after the initial starbursting phase is over (Cen 2011). The black holes formed in this manner, however, through pseudobulge evolution may not lie along the $M-\sigma$ relation (Kormendy et al. 2011).

7 CONCLUSION

(i) We have detected radio emission at 1280 MHz from five of the twelve bulgeless galaxies in our sample. Of these five galaxies, two galaxies, NGC 3445 and NGC 4027, show strong radio emission associated with their disks. Both galaxies are closely interacting with nearby companion galaxies and the radio emission is mainly due to the tidally triggered disk star formation. NGC 4027 also shows some nuclear radio emission. In the remaining three galaxies, the emission was patchy and due to localized star forming regions in their disks.
(ii) Both NGC 3445 and NGC 4027 have Hα disk emission associated with star formation along their spiral arms. The radio emission closely follows the Hα emission. The nuclear optical spectroscopy suggests that there is ongoing nuclear star formation in both NGC 3445 and NGC 4027; it is possibly associated with the formation of nuclear star clusters. No AGN emission lines were detected in the optical spectra of either galaxy.
(iii) The optical R band images of both NGC 3445 and NGC 4027 show concentrations of mass in their nuclear regions. This may represent small bulges in early stages of formation. The close tidal interactions has led to the formation of extended spiral structure and star formation which contribute to the build-up of nuclear mass. In NGC 4027 there is an oval distortion that may represent a pseudobulge. Thus close tidal interactions, rather than internal processes, may be important for bulge formation and disk evolution in low luminosity, bulgeless galaxies.

ACKNOWLEDGMENTS

We thank the GMRT staff for help in the observations. The GMRT is operated by the National Center for Radio Astrophysics of the Tata Institute of Fundamental Research. We also thank the staff of HCT, IAO for the support during the observations. This publication makes use of data products from the Two Micron All Sky Survey, which is a joint project of the University of Massachusetts and the Infrared Processing and Analysis Center/California Institute of Technology, funded by the National Aeronautics and Space Administration and the National Science Foundation. This research has made use of the NASA/IPAC Extragalactic Database (NED) which is operated by the Jet Propulsion Laboratory, California Institute of Technology, under contract with the National Aeronautics and Space Administration.

REFERENCES

Baggett W. E., Baggett S. M., Anderson K. S. J., 1998, AJ, 116, 1626
Banerjee A., Matthews L. D., Jog C. J., 2010, New A, 15, 89
Bell E. F., 2003, ApJ, 586, 794
Boissier S., Gil de Paz A., Boselli A., Madore B. F., Buat V., Cortese L., Burgarella D. e. a., 2007, ApJS, 173, 524
Böker T., Laine S., van der Marel R. P., Sarzi M., Rix H., Ho L. C., Shields J. C., 2002, AJ, 123, 1389
Böker T., Lisenfeld U., Schinnerer E., 2003, A&A, 406, 87
Böker T., Sarzi M., McLaughlin D. E., van der Marel R. P., Rix H., Ho L. C., Shields J. C., 2004, AJ, 127, 105
Böker T., Stanek R., van der Marel R. P., 2003, AJ, 125, 1073
Boselli A., Ciesla L., Cortese L., Buat V., Boquien M., Bendo G. J., Boissier S. e. a., 2012, A&A, 540, A54
Brook C. B., Governato F., Roškar R., Stinson G., Brooks A. M., Wadsley J., Quinn T., Gibson B. K., Snaith O., Pilkington K., House E., Pontzen A., 2011, MNRAS, pp 595–+
Brook C. B., Stinson G., Gibson B. K., Roškar R., Wadsley J., Quinn T., 2012, MNRAS, 419, 771
Cao C., Wu H., 2007, AJ, 133, 1710
Cen R., 2011, ArXiv e-prints
Combes F., Debbasch F., Friedli D., Pfenniger D., 1990, A&A, 233, 82
Daddi E., Alexander D. M., Dickinson M., Gilli R., Renzini A., Elbaz D., Cimatti A., Chary R., Frayer D., Bauer F. E., Brandt W. N., Giavalisco M., Grogin N. A., Huynh M., Kurk J., Mignoli M., Morrison G., Pope A., Ravindranath S., 2007, ApJ, 670, 173
Das M., Vogel S. N., Verdoes Kleijn G. A., O'Dea C. P., Baum S. A., 2005, ApJ, 629, 757
de Blok W. J. G., 2005, ApJ, 634, 227
D'Onghia E., Burkert A., 2004, ApJ, 612, L13
Ferrarese L., Merritt D., 2000, ApJ, 539, L9
Filippenko A. V., Ho L. C., 2003, ApJ, 588, L13
Filippenko A. V., Ho L. C., Sargent W. L. W., 1993, ApJ, 410, L75
Ganda K., Peletier R. F., Balcells M., Falcón-Barroso J., 2009, MNRAS, 395, 1669
Gebhardt K., Bender R., Bower G., Dressler A., Faber S. M., Filippenko A. V., Green R., Grillmair C., Ho L. C., Kormendy J., Lauer T. R., Magorrian J., Pinkney J., Richstone D., Tremaine S., 2000, ApJ, 539, L13
Gil de Paz A., Boissier S., Madore B. F., Seibert M., Joe Y. H., Boselli A., Wyder T. K., Thilker D., Bianchi L., Rey S.-C., Rich R. M. e. a., 2007, ApJS, 173, 185
Gil de Paz A., Madore B. F., Boissier S., Swaters R., Popescu C. C., Tuffs R. J., Sheth K., Kennicutt Jr. R. C., Bianchi L., Thilker D., Martin D. C., 2005, ApJ, 627, L29
Gliozzi M., Satyapal S., Eracleous M., Titarchuk L., Cheung C. C., 2009, ApJ, 700, 1759
Governato F., Brook C., Mayer L., Brooks A., Rhee G., Wadsley J., Jonsson P., Willman B., Stinson G., Quinn T., Madau P., 2010, Nature, 463, 203
Gültekin K., Richstone D. O., Gebhardt K., Lauer T. R., Tremaine S., Aller M. C., Bender R., Dressler A., Faber S. M., Filippenko A. V., Green R., Ho L. C., Kormendy J., Magorrian J., Pinkney J., Siopis C., 2009, ApJ, 698, 198
Heckman T. M., Kauffmann G., Brinchmann J., Charlot S., Tremonti C., White S. D. M., 2004, ApJ, 613, 109
James P. A., Shane N. S., Beckman J. E., Cardwell A., Collins C. A., Etherton J., de Jong R. S., Fathi K., Knapen J. H., Peletier R. F., Percival S. M., Pollacco D. L., Seigar M. S., Stedman S., Steele I. A., 2004, A&A, 414, 23
Karachentsev I. D., Makarov D. I., Sharina M. E., Dolphin A. E., Grebel E. K., Geisler D., Guhathakurta P., Hodge P. W., Karachentseva V. E., Sarajedini A., Seitzer P., 2003, A&A, 398, 479
Kautsch S. J., 2009, PASP, 121, 1297
Kennicutt Jr. R. C., 1998, ApJ, 498, 541
Kinney A. L., Bohlin R. C., Calzetti D., Panagia N., Wyse R. F. G., 1993, ApJS, 86, 5
Kormendy J., Bender R., Cornell M. E., 2011, Nature, 469, 374
Kormendy J., Drory N., Bender R., Cornell M. E., 2010, ApJ, 723, 54
Kormendy J., Fisher D. B., 2008, in J. G. Funes & E. M. Corsini ed., Formation and Evolution of Galaxy Disks Vol. 396 of Astronomical Society of the Pacific Conference Series, Secular Evolution in Disk Galaxies: Pseudobulge Growth and the Formation

of Spheroidal Galaxies. pp 297–+
Kormendy J., Freeman K. C., 2004, in S. Ryder, D. Pisano, M. Walker, & K. Freeman ed., Dark Matter in Galaxies Vol. 220 of IAU Symposium, Scaling Laws for Dark Matter Halos in Late-Type and Dwarf Spheroidal Galaxies. pp 377–+
Kormendy J., Kennicutt Jr. R. C., 2004, ARA&A, 42, 603
Martinez-Valpuesta I., Shlosman I., 2004, ApJ, 613, L29
Matthews L. D., Gallagher III J. S., 2002, ApJS, 141, 429
McAlpine W., Satyapal S., Gliozzi M., Cheung C. C., Sambruna R. M., Eracleous M., 2011, ApJ, 728, 25
Neumayer N., Walcher C. J., Andersen D., Sánchez S. F., Böker T., Rix H., 2011, MNRAS, pp 271–+
Oke J. B., 1990, AJ, 99, 1621
Peterson B. M., Bentz M. C., Desroches L.-B., Filippenko A. V., Ho L. C., Kaspi S., Laor A., Maoz D., Moran E. C., Pogge R. W., Quillen A. C., 2005, ApJ, 632, 799
Phookun B., Mundy L. G., Teuben P. J., Wainscoat R. J., 1992, ApJ, 400, 516
Pilyugin L. S., Vílchez J. M., Thuan T. X., 2010, ApJ, 720, 1738
Popescu C. C., Tuffs R. J., Völk H. J., Pierini D., Madore B. F., 2002, ApJ, 567, 221
Raha N., Sellwood J. A., James R. A., Kahn F. D., 1991, Nature, 352, 411
Ramya S., Prabhu T. P., Das M., 2011, MNRAS, 418, 789
Ravindranath S., Prabhu T. P., 1998, AJ, 115, 2320
Roussel H., Vigroux L., Bosma A., Sauvage M., Bonoli C., Gallais P., Hawarden T., Lequeux J., Madden S., Mazzei P., 2001, A&A, 369, 473
Salucci P., Persic M., 1997, in M. Persic & P. Salucci ed., Dark and Visible Matter in Galaxies and Cosmological Implications Vol. 117 of Astronomical Society of the Pacific Conference Series, Dark Halos around Galaxies. pp 1–+
Satyapal S., Böker T., Mcalpine W., Gliozzi M., Abel N. P., Heckman T., 2009, ApJ, 704, 439
Satyapal S., Vega D., Heckman T., O'Halloran B., Dudik R., 2007, ApJ, 663, L9
Sellwood J. A., Wilkinson A., 1993, Reports on Progress in Physics, 56, 173
Seth A., Agüeros M., Lee D., Basu-Zych A., 2008, ApJ, 678, 116
Shields J. C., Walcher C. J., Böker T., Ho L. C., Rix H., van der Marel R. P., 2008, ApJ, 682, 104
Silk J., Rees M. J., 1998, A&A, 331, L1
Smith B. J., Giroux M. L., Struck C., Hancock M., 2010, AJ, 139, 1212
Smith B. J., Struck C., Hancock M., Appleton P. N., Charmandaris V., Reach W. T., 2007, AJ, 133, 791
Walcher C. J., van der Marel R. P., McLaughlin D., Rix H.-W., Böker T., Häring N., Ho L. C., Sarzi M., Shields J. C., 2005, ApJ, 618, 237
Waller W. H., 1990, PASP, 102, 1217
Watson L. C., Schinnerer E., Martini P., Böker T., Lisenfeld U., 2011, ApJS, 194, 36
White S. D. M., Rees M. J., 1978, MNRAS, 183, 341
Young J. S., Xie S., Tacconi L., Knezek P., Viscuso P., Tacconi-Garman L., Scoville N., Schneider S., Schloerb F. P., Lord S., Lesser A., Kenney J., Huang Y.-L., Devereux N., Claussen M., Case J., Carpenter J., Berry M., Allen L., 1995, ApJS, 98, 219
Zackrisson E., Bergvall N., Marquart T., Östlin G., 2006, A&A, 452, 857

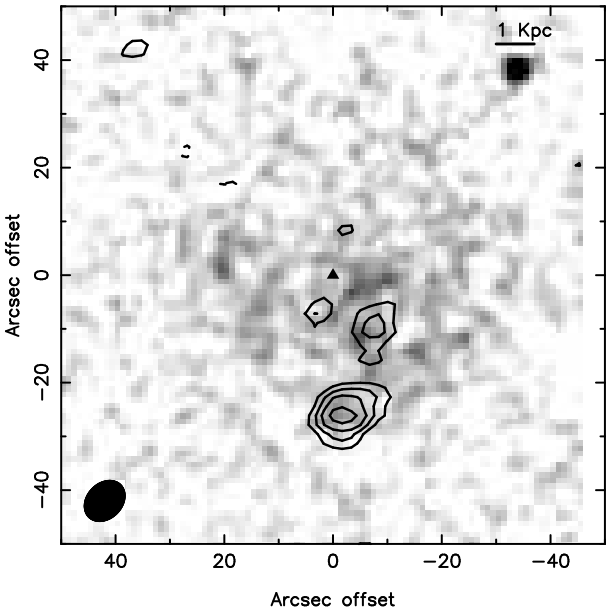

Figure 1. Figure shows the contours of the GMRT 1280 MHz radio continuum map of NGC 4299 superimposed on the 2MASS near-IR image of the galaxy. The peak radio flux is 1.4 $mJy\ beam^{-1}$ and the $beam \sim 7.3''$. The contours are 2, 3, 4, 5, 6 times the noise level which is 0.25 $mJy\ beam^{-1}$. The galaxy center is marked with a filled triangle. Note that the emission is offset from the galaxy center and lies mainly south of the nucleus in the disk.

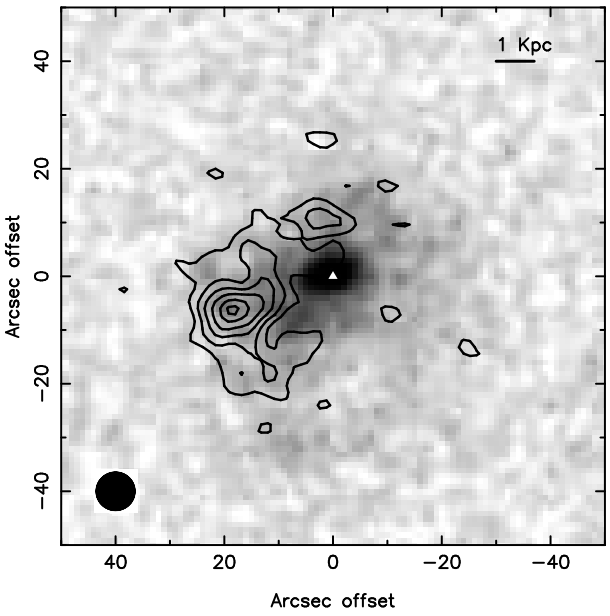

Figure 2. Figure shows the contours of the natural weighted GMRT 1280 MHz radio continuum map of NGC 3445 superimposed on the 2MASS near-IR image of the galaxy. The peak radio flux is 2 $mJy\ beam^{-1}$ and the $beam \sim 8''$. The contours are 4, 6, 8, 10, 12 times the noise level which is 0.15 $mJy\ beam^{-1}$. The galaxy center is marked with a filled triangle. Note that most of the emission is offset from the center of the galaxy and lies mainly east of the nucleus.

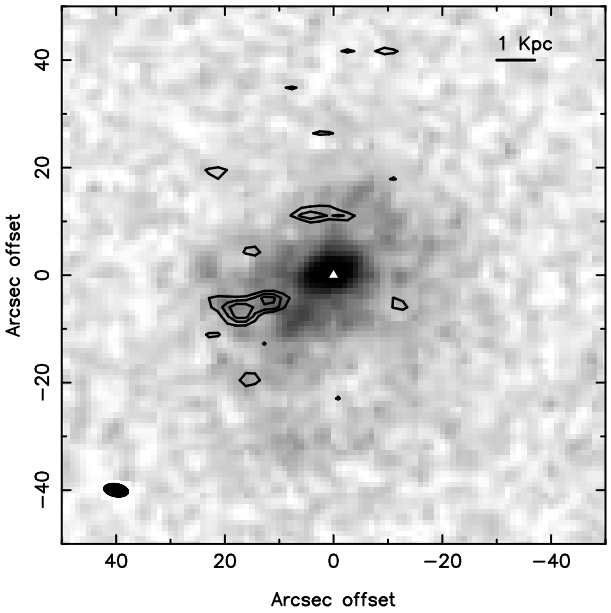

Figure 3. Figure shows the contours of the uniformly weighted (or high resolution) 1280 MHz radio continuum map of NGC 3445 superimposed on the 2MASS near-IR image of the galaxy. The peak radio flux is 2 *mJy beam*$^{-1}$ and the *beam* $\sim$ 5.5″ × 3.3″. The contours are 0.6, 0.8, 1 mJy *beam*$^{-1}$; this is 4, 5.7 and 7 times the noise level which is 0.14 *mJy beam*$^{-1}$. The high density emission is offset from the galaxy center and lies mainly east and north of the nucleus.

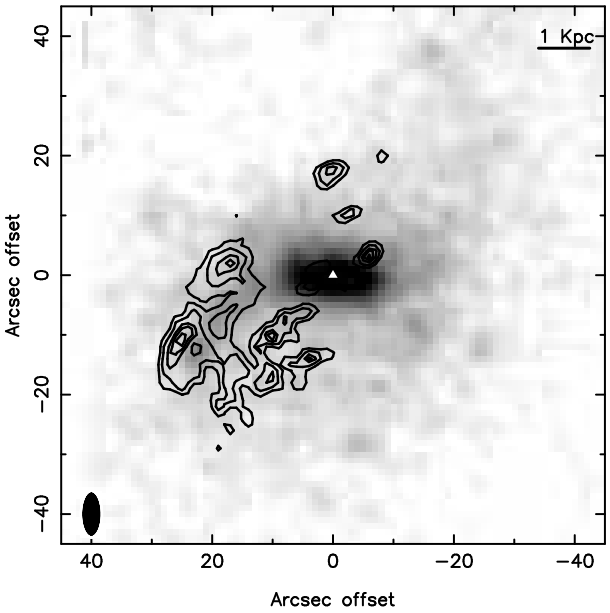

Figure 5. Figure shows the contours of the uniform weighted (robust 0) GMRT 1280 MHz radio continuum map of NGC 4027 superimposed on the 2MASS near-IR image of the galaxy. The peak radio flux is $\sim$ 1.9 *mJy beam*$^{-1}$ (*beam* $\sim$ 5.7″) and is located in the disk. The contours are 12, 14, 16, 17, 18 times the noise level which is 0.1 *mJy beam*$^{-1}$. Emission is mostly associated with knots of star formation in the southern spiral arm.

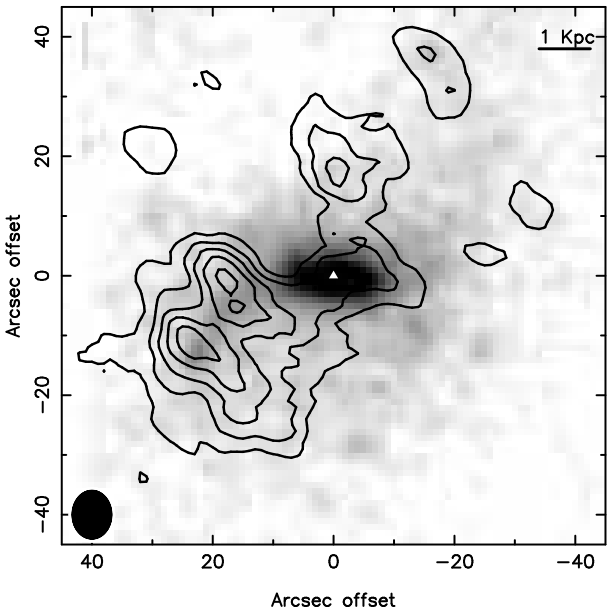

Figure 4. Figure shows the contours of the natural weighted GMRT 1280 MHz radio continuum map of NGC 4027 superimposed on the 2MASS near-IR image of the galaxy. The peak radio flux is $\sim$ 3.5 *mJy beam*$^{-1}$ where *beam* $\sim$ 8″; it is located in the disk and not the nucleus. The contours are 8, 10, 12, 14, 16, 18 times the noise level which is 0.29 *mJy beam*$^{-1}$. The galaxy center is marked with a filled triangle. The radio emission is mostly associated with the spiral arms and the southern arm is more prominent.

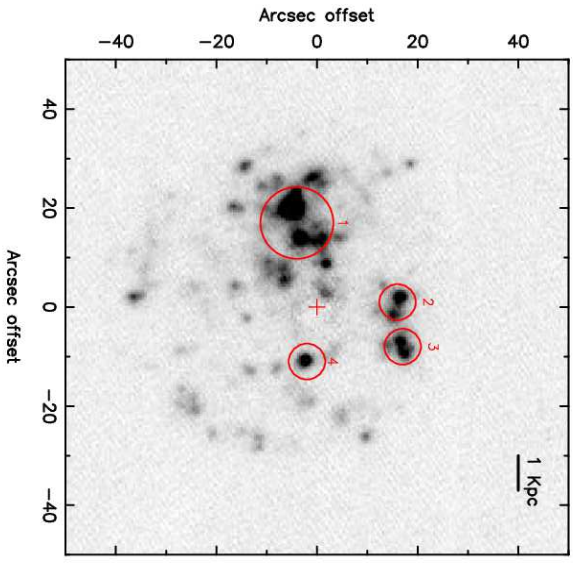

Figure 6. The figure shows the Hα image of NGC 3445 with the main star forming regions circled in red (see Table 3). The emission is mainly concentrated along the southern spiral arm and associated with star formation in the disk. The galaxy center is marked with a red cross and does not seem to show much Hα emission.

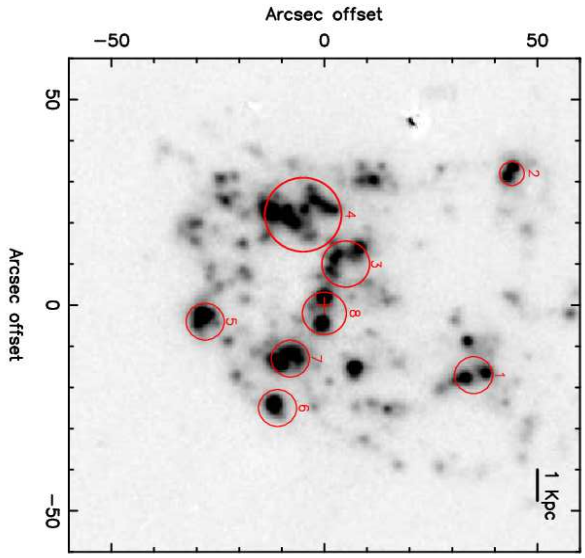

Figure 7. The above figure shows the Hα image of NGC 4027; the galaxy center is marked with a red cross and the main star forming regions circled in red (see Table 3). A large part of the emission is associated with the southern spiral arm and lies southeast of the galaxy nucleus. There are also star forming regions associated with the galaxy center and the northern spiral arm.

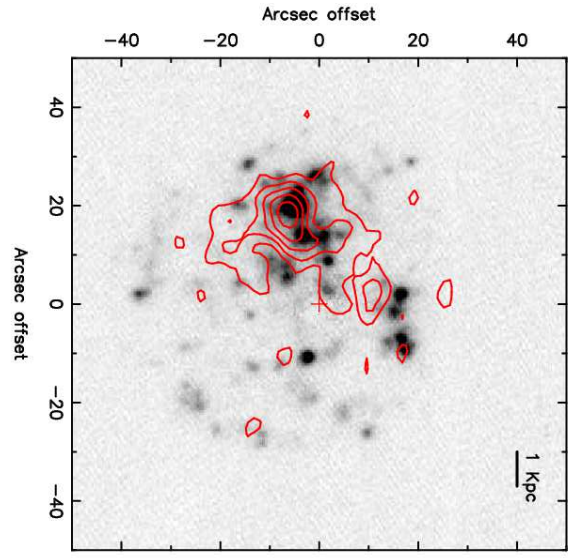

Figure 8. The figure shows the Hα image of NGC 3445 with radio continuum contours overlaid in red. The radio emission mostly traces the Hα emission, but is more extened to the south.

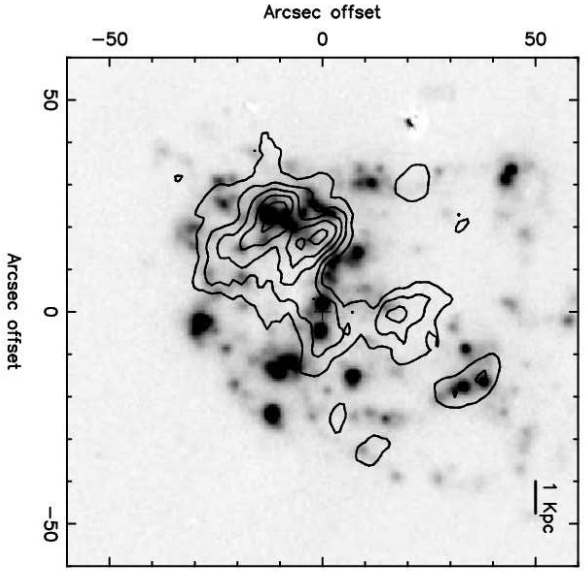

Figure 9. The figure shows the Hα image of NGC 4027 with radio continuum contours overlaid in red. The radio emission follows the Hα emission and traces the southern and northern spiral arms.

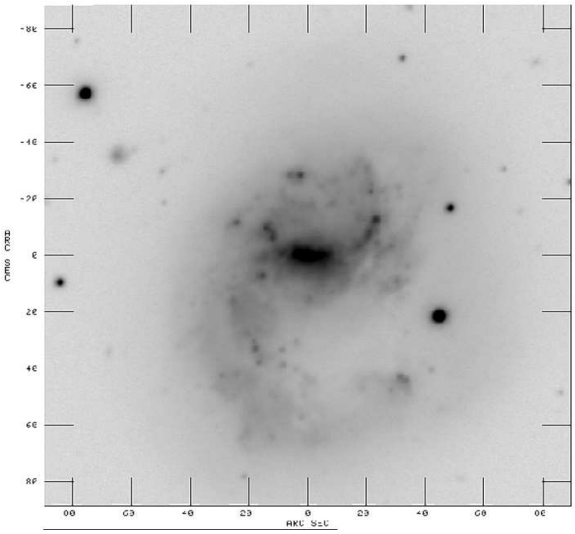

Figure 10. Residual R band image of NGC 4027 derived from the Hα image of the galaxy. The central oval distortion is possibly a pseudobulge that developed from the buckling of a small bar triggered through interaction with NGC 4027 A.

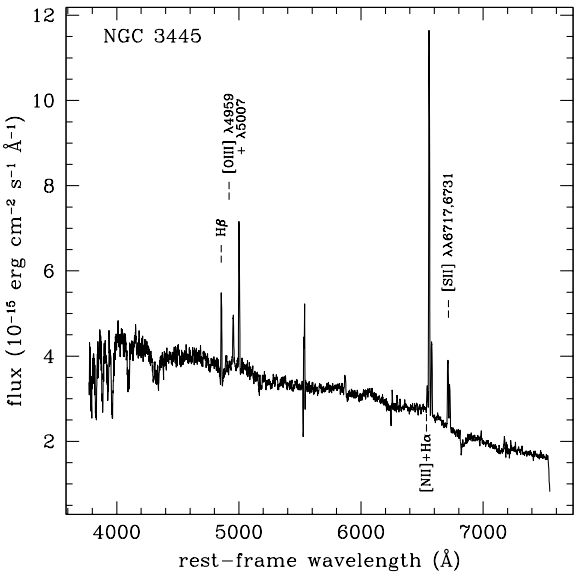

Figure 11. Spectrum of NGC 3445 obtained from HFOSC installed in HCT. The spectrum covers the blue region obtained from grism # 7 (3700-7800 Å) having a dispersion of ∼ 1.45 Å pix^{-1} at central wavelength 5600 Å.

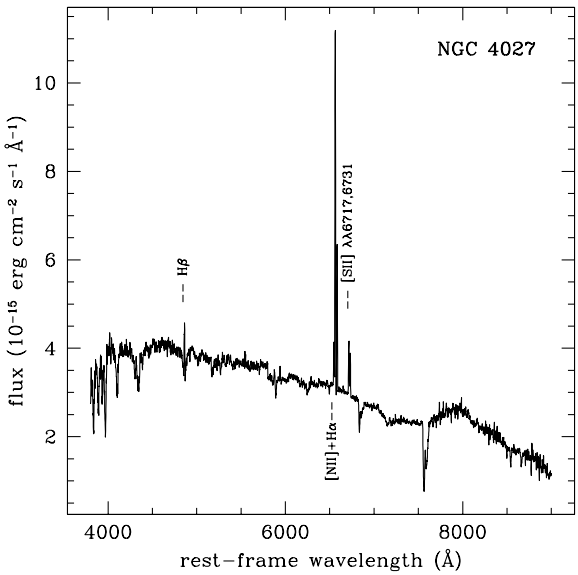

Figure 13. Spectrum of NGC 4027 obtained from HFOSC installed in HCT. The spectrum is a combined spectrum of grism #7 and #8 covering both the blue (3700-7800 Åwith dispersion of ∼ 1.45 Å pix^{-1} at central wavelengths) and red region (5200-9100 Åwith a dispersion of ∼ 1.25 Å pix^{-1} at central wavelengths). Notice the absence of Oxygen lines like [O II], ø3 or [O I].

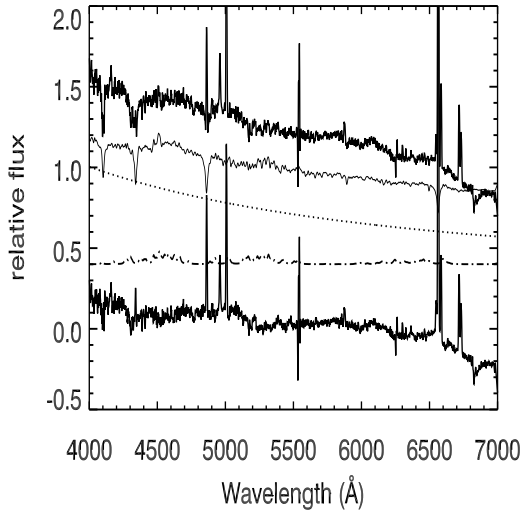

Figure 12. The figure shows the observed spectrum (thick black line) of NGC 3445 and the best fitting starburst99 template of age ∼ 700 Myr (thin solid line). The dotted line is the power law template and the dot-dashed line is the Fe II template. The difference between the observed spectrum and the combined model, power law and Fe II templates. This residual spectrum is used for estimation of the integrated fluxes of each element.

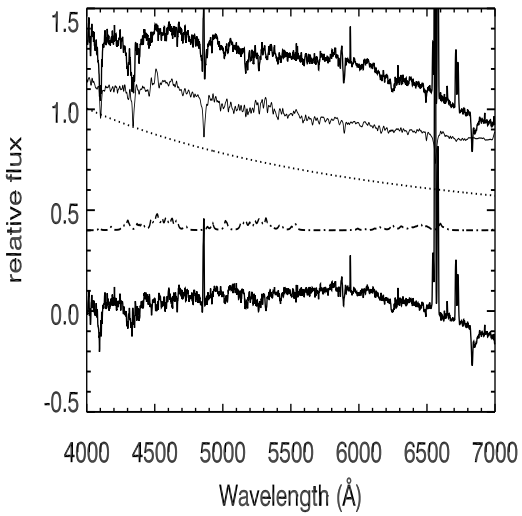

Figure 14. Figure is similar to Figure 12 but is for the galaxy NGC 4027. The best fit age for the underlying stellar population is ∼ 1 Gyr.